CCS Chemistry

RESEARCH ARTICLE

Received: Sept. 21, 2020 | Accepted: Nov. 11, 2020 | Corrected: Mar. 8, 2021

Synthesis of Iron-Carbide Nanoparticles: Identification of the Active Phase and Mechanism of Fe-Based Fischer–Tropsch Synthesis

Huabo Zhao[1†], Jin-Xun Liu[2†], Ce Yang[3†], Siyu Yao[1], Hai-Yan Su[4], Zirui Gao[1], Mei Dong[5], Junhu Wang[6a], Alexandre I. Rykov[6a], Jianguo Wang[5], Yanglong Hou[3*], Wei-Xue Li[2*] & Ding Ma[1*]

[1]College of Chemistry and Molecular Engineering, Peking University, Beijing 100871, [2]Department of Chemical Physics, School of Chemistry and Materials Science, Hefei National Laboratory for Physical Sciences at the Microscale, iCHEM, University of Science and Technology of China, Hefei 230026, [3]Department of Materials Science and Engineering, College of Engineering, Peking University, Beijing 100871, [4]School of Chemical Engineering and Energy Technology, Dongguan University of Technology, Dongguan 523808, [5]State Key Laboratory of Coal Conversion, Institute of Coal Chemistry, Chinese Academy of Sciences, Taiyuan 030001, [6]Center for Advanced Mössbauer Spectroscopy, Dalian Institute of Chemical Physics, Chinese Academy of Sciences, Dalian 116023[a]

**Corresponding authors: hou@pku.edu.cn; wxli70@ustc.edu.cn; dma@pku.edu.cn; †H. Zhao, J.-X. Liu, and C. Yang contributed equally to this work.*

Cite this: *CCS Chem.* **2020**, *2*, 2712–2724

Despite the extensive study of the Fe-based Fischer–Tropsch synthesis (FTS) over the past 90 years, its active phases and reaction mechanisms are still unclear due to the coexistence of metals, oxides, and carbide phases presented under realistic FTS reaction conditions and the complex reaction network involving CO activation, C–C coupling, and methane formation. To address these issues, we successfully synthesized a range of pure-phase iron and iron-carbide nanoparticles (Fe, Fe_5C_2, Fe_3C, and Fe_7C_3) for the first time. By using them as the ideal model catalysts on high-pressure transient experiments, we identified unambiguously that all the iron carbides are catalytically active in the FTS reaction while Fe_5C_2 is the most active yet stable carbide phase, consistent with density functional theory (DFT) calculation results. The reaction mechanism and kinetics of Fe-based FTS were further explored on the basis of those model catalysts by means of transient high-pressure stepwise temperature-programmed surface reaction (STPSR) experiments and DFT calculations. Our work provides new insights into the active phase of iron carbides and corresponding FTS reaction mechanism, which is essential for better iron-based catalyst design for FTS reactions.

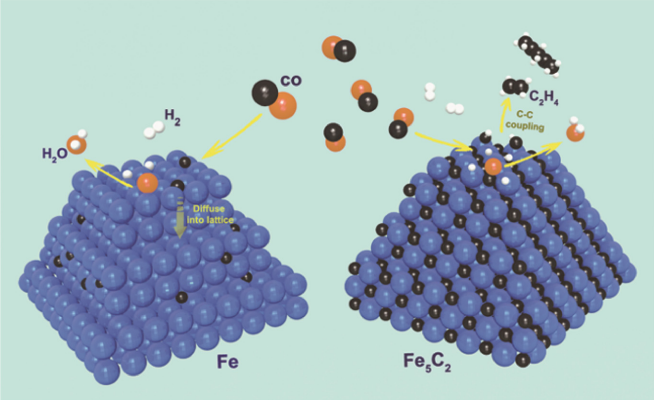

Keywords: Fischer–Tropsch synthesis, iron carbides, active phase, reaction mechanism

DOI: 10.31635/ccschem.020.202000555
CCS Chem. **2020**, *2*, 2712–2724

Introduction

Fischer–Tropsch synthesis (FTS) receives increasing attention because synthesis gas (syngas) can be obtained from coal, biomass, and shale gas, which becomes particularly important for the production of alternative fuel and chemicals.[1,2] Despite the extensive exploration of Fe-based catalysts over the past 90 years, its active phases and reaction mechanisms are still controversial.[3] The typical iron catalysts, usually produced from thermal reduction and successive activation of iron oxide precursors, contain different phases, including metals, oxides, and carbides, produced during the pretreatment of the catalysts by carbon-containing gases such as CO.[4–10] The phase evolution of the iron catalysts during the FTS reaction is even more complicated, and in most cases, a mixture of different phases occurred.[11–15] To address this issue, various types of metal or metal carbides were prepared.[16–22] Metallic iron[23,24] and various phases of iron carbides had all been claimed to be active.[4,6,25–38] The complication for FTS comes also from the complexity of the reaction network itself, including CO activation, C–C bond formation, and methane formation.[32,39–45] However, the reaction performance dependence on catalyst phases of iron and carbides as well as the catalytic mechanism behind was still elusive, hindering better Fe-based catalyst design for FTS.

To address these challenging issues, for the first time, we have successfully synthesized a variety of pure-phase iron and iron-carbide catalysts with similar particle size, including Fe, Fe_7C_3, Fe_3C, Fe_5C_2, and so forth, which allow us to identify their initial and intrinsic activities as well as the structural evolution of iron-based catalysts during FTS. At the same time, we developed a new experiment, a transient high-pressure stepwise temperature-programmed surface reaction (STPSR) that enabled us to directly explore such complicated and challenging problems in FTS as fundamental knowledge about syngas activation, hydrocarbon and methane formation on pure-phase catalysts, which were previously unavailable. The comprehensive density functional theory (DFT) calculations revealed a deep insight into the intrinsic activity of iron metal and iron carbides on CO activation, C–C bond, and methane formation, rationalizing the kinetic and thermodynamic origin on the structural evolution of different iron-based catalysts during the FTS reaction. This deeper understanding of the active phase of iron-based catalysts and the corresponding FTS reaction mechanism is beneficial for rational design of more effective Fe-based catalysts on FTS by the synthesis of more Fe_5C_2 catalyst.

Experimental Methods

Synthesis of Fe_7C_3 and Fe_2C NPs

In a four-neck flask, 20 mL of *N*,*N*-dimethyloctadecylamine (for Fe_7C_3) or dodecylamine (for Fe_2C) was stirred sufficiently and degassed under 120 °C for 2 h. Then, the system was refilled with NH_3 and heated to 180 °C. After that, $Fe(CO)_5$ (0.7 mL, 5.0 mmol) was injected under NH_3 atmosphere and kept at this temperature for 30 min. A color change from orange to black was observed during the process, implying the decomposition of $Fe(CO)_5$ and the nucleation of Fe nanocrystals. Subsequently, the mixture was further heated to 350 °C (for Fe_7C_3) or 260 °C (for Fe_2C) at 10 °C/min and kept for 2 h before it was cooled down to room temperature. The product was washed with ethanol and hexane, and collected for further characterization. The as-synthesized nanoparticles (NPs) were kept in an Ar-filled glovebox to avoid exposure to air before further characterization. In the absence of NH_3, the NPs would be oxidized to iron oxide (Supporting Information Figures S1 and S2).

Synthesis of Fe_5C_2 and Fe NPs

In a four-neck flask, a mixture of octadecylamine (14.5 g) and Hexadecyltrimethylammonium bromide (CTAB) (0.113 g) was stirred sufficiently. Then, the system was refilled with N_2 and heated to 180 °C. Following that, $Fe(CO)_5$ (0.5 mL, 3.6 mmol) was injected under a N_2 blanket. The mixture was kept at 180 °C for 10 min. A color change from orange to black was observed during the process, implying the decomposition of $Fe(CO)_5$ and the nucleation of Fe nanocrystals. Subsequently, the mixture was further heated to 350 °C (for Fe_5C_2) or 300 °C (for Fe) at 10 °C/min and kept for 10 min before it was cooled down to room temperature. The product was washed with ethanol and hexane, and was kept in an Ar-filled glovebox to avoid exposure to air before further characterization.

Preparation of supported catalyst

The NPs obtained from high-temperature liquid-phase synthesis had been washed with *n*-hexane and ethanol several times and dispersed in *n*-hexane under N_2 protection. Afterward, the dispersion of iron-carbide NPs was added into a certain amount of silica (N_2 adsorption–desorption isotherm is shown in Supporting Information Figure S3) under stirring. After evaporating the solvent at room temperature, the supported catalyst was prepared. The amount of iron determined by inductively coupled plasma (ICP) was around 8%.

Catalysis reaction

The catalytic performance of the catalysts was evaluated in a fixed bed reactor. About 80 mg catalyst was loaded in a quartz-lined stainless steel reactor. The feed gas was a mixture of 32% CO, 64% H_2, and 4% Ar. In a typical reaction, the pressure and gas flow rate were set for 30 bar and 20 mL/min (gas hourly space velocity,

DOI: 10.31635/ccschem.020.202000555
CCS Chem. **2020**, *2*, 2712–2724

GHSV = 15,000 mL/g·h), respectively. Then, the reaction tube was heated from room temperature to 270 °C at 5 °C/min, and the reaction was conducted at 270 °C. It is worth noting that no reduction or carburizing pretreatment was carried out before the reaction. The gas-phase products were analyzed by an Agilent 6890 gas chromatography (GC) equipped with a flame ionization detector (FID) and thermal conductivity detector (TCD), with 4% Ar as inert standard. The heavier hydrocarbons were cooled down and collected in a trap, and analyzed offline by an Agilent GC 7820, with a HP-5 capillary column and FID. The products selectivity was calculated on a carbon basis.

STPSR experiment

Prior to the STPSR experiments, the Fe catalyst was treated in H_2 (20 mL/min) and the Fe_5C_2 catalyst was treated in 10% C_2H_4/H_2 mixture at 300 °C for 2 h to remove the surface contaminants. After cooling down to room temperature, the gas flow was switched to synthesis gas of 20 mL/min, and the pressure was raised to 30 bar. Then, the reactor was heated to 150 °C at 20 °C/min, and kept steady for 2 h. Afterward, the temperature was elevated 20 °C higher and held for 2 h at that temperature. The process was repeated until the reaction temperature reached 270 °C. A Pfeiffer Omnistar mass spectrometer (MS) was used to analyze the reactants and products online. The M/e value detected as follows: 2 for hydrogen; 15 for methane; 18 for water; 26, 27, and 30 for C_2 products (acetylene, ethylene, and ethane); 28 for CO; 42 for C_3; 44 for CO_2; 56 for C_{4+}; and 70 for C_{5+}.

Catalyst characterization

The transition electron microscopy (TEM) experiments were conducted at a FEI Tecnai F30 transmission electron microscope (HRTEM) operating at 300 keV. The X-ray photoelectron spectroscopy (XPS) experiments were carried out on an AXIS Ultra imaging photoelectron spectrometer with Al kα as X-ray source. The binding energy of graphite carbon was calibrated to 284.8 eV. Powder X-ray diffraction (XRD) data were collected at a Rigaku D/Max-2400 equipped with Cu Al Kα radiation. The Raman characterizations were performed on a Renishaw 1000 Raman imaging microscope system with an excitation wavelength of 632.8 nm. The ^{57}Fe Mössbauer effect spectra of as-synthesized iron-carbide NPs were collected by a Topological 500A spectrometer and a proportional counter at room temperature. The γ radiative source was a ^{57}Co (Rh) moving with constant acceleration mode. The X-ray absorption fine structure (XAFS) spectra were collected at beam line 14 W of Shanghai Synchrotron Facility (SSRF) in transmission mode with a Si (111) monochromator. The samples for characterization were prepared and transferred under protection of Ar. As metallic iron and iron carbide were very sensitive to oxidation, the oxidation of the sample was sometimes unavoidable. For TEM study, the catalyst used was passivated in 0.5% O_2 in Ar at room temperature for 1 h before the measurement.

Calculation

Spin-polarized DFT calculations have been performed by using the Vienna ab initio simulation package (VASP).[46,47] Throughout the calculations, projector augmented wave (PAW) potential[48] and the generalized gradient approximation (GGA) with the Perdew–Burke–Ernzerhof (PBE) exchange–correlation functional[49] were adopted. The planewave cutoff energy was set by 400 eV. The force and energy convergence standards were 0.02 eV/Å and 1×10^{-4} eV, respectively. Monkhorst–Pack[50] *k*-points sampling of $3 \times 7 \times 7$ and $10 \times 10 \times 10$ were adopted for Fe_5C_2 and Fe bulk calculations with monoclinic (space group C2/c) and body-centered cubic (BCC) crystal structures, respectively. The optimized lattice constant of Fe_5C_2 is $a = 11.55$ Å, $b = 4.50$ Å, and $c = 4.99$ Å with $\beta = 97.6°$, which are consistent with experimental findings that $a = 11.59$ Å, $b = 4.58$ Å, and $c = 5.06$ Å with $\beta = 97.75°$.[51] The calculated lattice constant (2.83 Å) for Fe with BCC crystal structure also agreed very well with the experiment.[52]

Fe-terminated Fe_5C_2 (100) surface was simulated by a slab of seven-layered Fe atoms and three-layered C atoms. In the calculations, the topmost four Fe and one C layers were fully relaxed, whereas the remaining atoms were fixed in their bulk positions. For the BCC-Fe (310) surface, a 10-layered Fe atoms slab model was used, and only the top five Fe layers were allowed to relax. A $p(2 \times 2)$ unit cell was utilized for the two slab models considered. We have used Monkhorst–Pack mesh *k*-points of $3 \times 3 \times 1$ for Fe_5C_2 (100) and $5 \times 5 \times 1$ for the BCC-Fe (310) surface. The vacuum region along the *z* direction was specified by 15 Å, and the dipole correction was considered in our calculations. Force reversed method[53] was used to locate the transition states (TSs), and a force tolerance of 0.03 eV/Å was applied without zero-point correction. Some TSs along the minimum-energy reaction pathways were also reaffirmed by using the climbing image-nudged elastic band (CI-NEB) method.[54] For a given elementary reaction, we considered the separately adsorption of intermediates at their most favorable adsorption sites as the initial and final states for the reaction barrier calculations.

Results and Discussion

In fabrication of both Fe_7C_3 and Fe_2C NPs, NH_3 was chosen as the atmosphere as well as the inducing agent while $Fe(CO)_5$ was used as the precursor. In particular, Fe_7C_3 NPs were obtained in *N*,*N*-dimethyloctadecylamine solvent under 350 °C for 2 h, and Fe_2C NPs were produced in dodecylamine solvent under 260 °C for 2 h (see Supporting Information). α-Fe

DOI: 10.31635/ccschem.020.202000555
CCS Chem. **2020**, *2*, 2712–2724

and Fe_5C_2 NPs were synthesized via a bromide-induced process as described elsewhere.[19] Figures 1a–1h present the powder XRD patterns and corresponding TEM images of as-synthesized Fe_7C_3, Fe_2C, Fe_5C_2, and α-Fe NPs. According to the XRD results, the peaks in each sample consistent with the standard patterns, which suggests the generation of a single phase in each of the four samples. Furthermore, TEM images of the four samples indicated that they were all spherical NPs with diameters around 18 nm.

The XAFS and Mössbauer spectra data also supported this conclusion. Fe K-edge XANES suggested that the iron-carbide particles exhibit very low oxidation states as compared with the metallic Fe foil. The relatively low-frequency oscillation of the postedge features indicated that the Fe central atom had neighbors with small bond lengths. Further extended XAFS (EXAFS) fitting results confirmed that all of the Fe-carbide particles synthesized had Fe–C coordination shells near 2.0 Å. The average first Fe–Fe shell bond length expanded from 2.46 to around 2.60 Å due to the incorporation of carbon into the BCC lattice of α-Fe (Figures 2a and 2b). Furthermore, no features of Fe oxides and Fe were observed, suggesting all the particles were pure carbide. (The Mössbauer spectra and corresponding fitting results are shown in Supporting Information Figure S4 and Table S1.) The sextet peaks indicated the formation of Fe_2C, Fe_7C_3, and Fe_5C_2 NPs, while the weak doublet peaks in Fe_5C_2 suggested that the Fe_5C_2 NPs might have better crystallinity compared with Fe_2C and Fe_7C_3. Therefore, the single-phase nature of these α-Fe and iron-carbide NPs, along with their similar morphology, provides us with an ideal platform for the investigation of their intrinsic catalytic behavior and structural evolution in the FTS process. At the same time, because the cementite (Fe_3C) was reported to have poor activity in FTS,[30,32] it was not discussed in this work.

The α-Fe and iron-carbide NPs were dispersed on silica support and directly used in the FTS reaction (3 MPa syngas, 270 °C). For a 40 h reaction, the product distribution on Fe and Fe_5C_2 was similar except Fe had higher C_{5+} selectivity (49%). Fe_2C had the highest selectivity toward CO_2 (22.7%), while Fe_2C and Fe_7C_3 showed considerably high selectivity of 20.1% and 19.5% toward methane, respectively (Supporting Information Figure S5). Both CO_2 and CH_4 are undesired products. CO conversion on prepared catalysts with time on stream is shown in Figure 3 with FTS activity shown in Table 1.

At the beginning, Fe_5C_2 exhibited the highest CO conversion (around 35%), followed by Fe_2C (29.5%) and Fe_7C_3 (22.5%), while α-Fe had the lowest CO conversion (15.2%). The initial CO reactivity reflected the intrinsic catalytic properties of Fe_2C, Fe_7C_3, and Fe_5C_2. With the reaction proceeding, the activities of the four catalysts showed different trends. For Fe_5C_2 and Fe_2C, the CO conversion decreased sharply in the first 6 h but

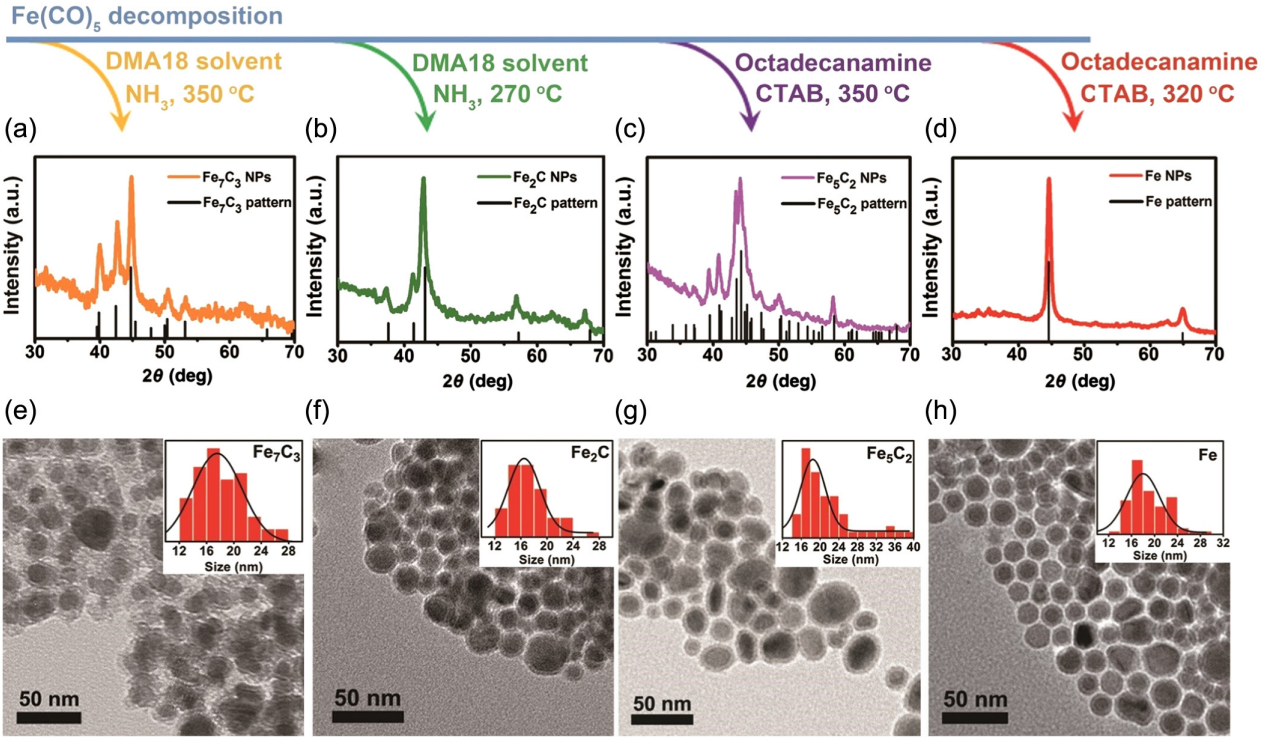

Figure 1 | *XRD patterns and TEM images of (a and e) Fe_7C_3, (b and f) Fe_2C, (c and g) Fe_5C_2, and (d and h) α-Fe NPs. It is clear from the TEM images and XRD profiles that all the obtained Fe and iron-carbide NPs have the pure-phase structure and similar size (around 18 nm).*

DOI: 10.31635/ccschem.020.202000555
CCS Chem. **2020**, *2*, 2712–2724

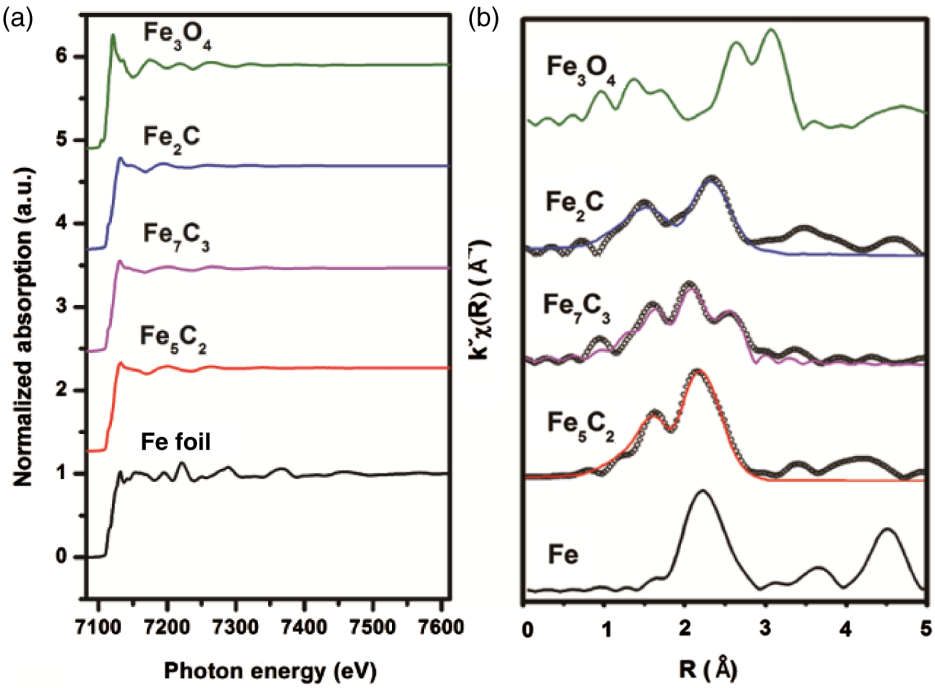

Figure 2 | *(a) XANES and (b) EXAFS spectra of Fe_5C_2, Fe_7C_3, and Fe_2C. The XANES and EXAFS spectra of Fe foil and standard pattern of Fe_3O_4 are shown by black and green curves, respectively. The curves composed by black circles in (b) indicate the experimental data of each iron carbide, and the colored curves indicate the simulation curves. The XAFS samples were prepared and transferred under protection of Ar.*

gradually stabilized later on. For Fe_7C_3, CO conversion dropped slightly in the first 5 h, and after a small increase, it became stabilized. On the contrary, that of the α-Fe catalyst increased rapidly in the first 7 h, and then remained almost constant afterward. When the conversion for all catalysts approached the steady state, Fe_5C_2 remained the most active with a conversion of 27%, and the activities of Fe_7C_3 and Fe (25% and 24%) were slightly lower, whereas Fe_2C became the least active (17%). The turnover frequency (TOF) and activity of those Fe-based catalysts are summarized in Table 1. Obviously, Fe_5C_2 had the highest initial- and steady-state activities (2.3 and 1.8 × 10^{-4} Mol_{CO}/g_{Fe}·s). After reaction, the morphologies of used Fe_5C_2 and Fe_2C catalysts were maintained with main phases transformed into a mixture of iron oxide and original carbide, whereas for Fe_7C_3, the formation of Fe_5C_2 was observed (Supporting Information Figures S6 and S7). Significantly, the main phase of used α-Fe catalyst was transformed into Fe_5C_2, in addition to Fe_3O_4 (Supporting Information Figure S6). There has always been a debate on whether and why metal and/or carbide is the active phase for FTS. To examine this, we chose Fe_5C_2 as a representative for the carbide phase and compared its catalytic behavior in the early stage of FTS with that of α-Fe catalyst. We designed a high-pressure STPSR apparatus to allow the observation of reaction kinetics at high pressure. This STPSR experiment enabled us to observe the masked information by steady-state reaction evaluation.[17,60,61]

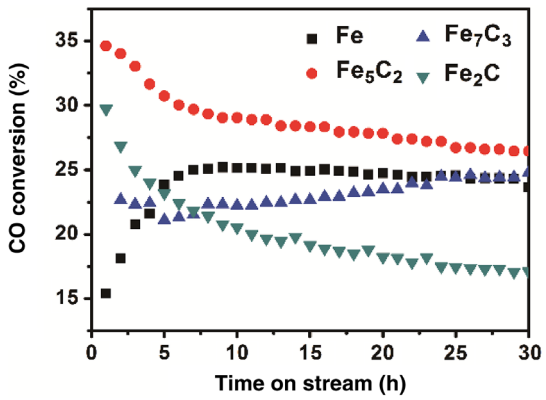

Figure 3 | *CO conversion as a function of time over Fe, Fe_2C, Fe_7C_3, and Fe_5C_2 catalysts (reaction conditions: 270 °C, 30 bar, 20 mL/min syngas).*

The formation of various products during the STPRS of syngas over the Fe_5C_2 catalyst is illustrated in Figure 4a. Before 150 °C, no products were formed, which indicates that syngas cannot be activated over Fe_5C_2 at temperatures below 150 °C. With the reaction temperature reaching 150 °C for 20 min, the formation of water, C_2 hydrocarbons (mostly acetylene and ethylene), and CO_2 were observed. When the temperature was raised to 170 °C, with the appearance of C_3 hydrocarbon, the

DOI: 10.31635/ccschem.020.202000555
CCS Chem. **2020**, *2*, 2712–2724

Table 1 | *The Surface-Specific Activity (TOF) and Metal-Mass-Based Activity (Activity) Excluded CO_2 Formation over Various Iron and Iron-Carbides Catalysts*

Catalysts	Temperature (°C)	Pressure (bar)	TOS (h)	TOF_{FTS} (s^{-1})	Activity (1×10^{-4} $Mol_{CO}/g_{Fe}.s$)	References
Fe	270	30	1	0.13	1.1	This work
Fe	270	30	30	0.20	1.7	This work
Fe_5C_2	270	30	1	0.29	2.3	This work
Fe_5C_2	270	30	30	0.22	1.8	This work
Fe_7C_3	270	30	1	0.16	1.6	This work
Fe_7C_3	270	30	30	0.18	1.7	This work
Fe_2C	270	30	1	0.16	1.8	This work
Fe_2C	270	30	30	0.09	1.0	This work
Fe_xO_y@C	270	20	—	—	0.31	[55]
Fe/SiO_2	270	20	—	—	0.20	[56]
Fe-in-CNT	270	50	—	—	2.5	[57]
25-Fe@C	340	20	—	0.11	4.9	[58]
RQ Fe	200	30	—	—	3.5	[59]

Abbreviations: TOF, turnover frequency; TOS, time on stream.

amount of water and C_2 formed was considerably high. Yet, to our surprise, methane was not detected until then. The MS signal for methane appeared only when the reaction temperature reached 190 °C. The formation of methane at a higher temperature than that of C_2 hydrocarbons indicates that the hydrogenation of monomers toward methane is kinetically less favorable than C–C coupling. When the temperature reached 210 °C, C_4 compounds appeared, followed by the formation of C_{5+} hydrocarbons 20 min later.

To our surprise, the STPSR profile of α-Fe catalyst showed a distinct behavior as compared with that of Fe_5C_2 (Figure 4b). At 150 °C, water formation was reproducibly observed, whereas no C_2 hydrocarbons could be detected in 2 h. Instead, C_2 hydrocarbon appeared only at around 10 min after the temperature reached 170 °C. The formation temperature of methane, C_3 alkane, and CO_2 was at least 190 °C. C_4 and C_5 formed at 210 and 230 °C, which was very similar to those of Fe_5C_2. Thus, although C_2 hydrocarbon on α-Fe formed at a higher temperature (170 °C) than that on Fe_5C_2 (150 °C), the formation of methane on both catalysts requires a temperature of 190 °C or higher. Namely, methane formation on both catalysts remains less favorable, compared with the formation of water and C_2 hydrocarbon. The formation of water in STPSR process is interesting as the preadsorbed water on the catalysts was removed through a pretreatment at 300 °C before STPSR. Therefore, the water can only be formed from the reaction between hydrogen and oxygen adsorbed on the catalyst. There are two possible sources for adsorbed oxygen, namely, either the product from CO dissociation or the contaminated molecular oxygen from the gas phase that was not removed by hydrogen pretreatment before STPSR. In fact, the latter oxygen source can be excluded by a H_2-STPSR experiment (Supporting Information Figure S8). This implies that the oxygen source of water on the α-Fe catalyst can only be the dissociated O from CO. Therefore, it is concluded that CO dissociation took place at 150 °C over Fe catalyst, which is also the case for the Fe_5C_2 catalyst.

Dissociated carbon would be hydrogenated, subsequently forming the hydrocarbons.[62,63] At 150 °C, the

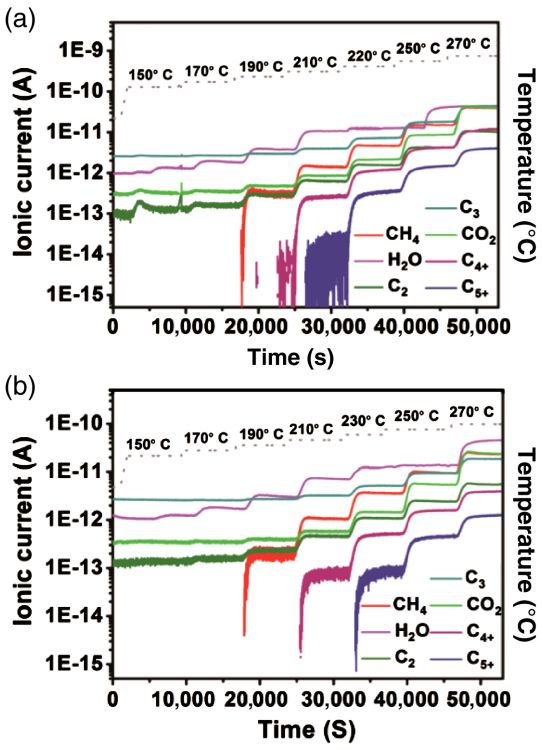

Figure 4 | *STPSR profile on (a) Fe_5C_2 and (b) Fe catalysts.*

DOI: 10.31635/ccschem.020.202000555
CCS Chem. **2020**, *2*, 2712–2724

formation of the hydrocarbons was observed on Fe_5C_2, but not on α-Fe within the first 2 h. This implies that dissociated carbon would accumulate on α-Fe, and might diffuse into the interstitial sites of the subsurface and the bulk α-Fe region, carburizing α-Fe toward carbide. Fe NPs can be easily carburized into iron carbides,[64] whereas the transformation from the single crystals and sheets of Fe to iron carbide is difficult,[65,66] which can be attributed to the difficulty for carbon atoms permeating into the interstitial sites formed by the close packing of Fe atoms. Thermodynamically, this is possible since the corresponding Gibbs free formation energy (−3.22 eV per chemical formula unit of Fe_5C_2 under FTS conditions) at this condition is exothermic (Section 8 in Supporting Information). The above hypothesis was confirmed by in situ XRD experiments under FTS reaction conditions (2 MPa syngas, Figure 5). It was found that under a syngas stream, α-Fe, which corresponds to a diffraction with a two-theta value of 35.3°, was gradually transformed to the iron-carbide phase (two-theta value of 34.8°, most like Fe_5C_2) when increasing the reaction temperature higher than 220 °C. Although the reaction condition was not exactly the same as in the STPSR experiments, this tells compellingly that in the FTS process, α-Fe is indeed apt to react with surface carbon from dissociated CO, forming iron carbide. Moreover, when we carburized the supported α-Fe catalyst with ethylene or the mixture of ethylene and hydrogen to get supported iron-carbide catalyst (Fe_5C_2, as evidenced by XRD (Figures 6b and 6c), we observed that the initial activity of the resulting carburized catalyst increased dramatically (Figure 6a), reaching 33%, very close to the initial activity of the pure-phase Fe_5C_2 catalyst. The activity evolution of the carburized Fe catalyst almost duplicated that of Fe_5C_2 catalyst, that is, it dropped gradually in the first few hours and became relatively stable after around 15 h of reaction. The induction period observed on the α-Fe catalyst could therefore be attributed to the process of carburization. Once the carburization was complete and Fe_5C_2 was formed, the resulting catalysts would showed a higher activity because of the higher intrinsic activity of Fe_5C_2.

For the drop of activity of Fe_5C_2 catalyst with reaction time (Figure 3), it was attributed to the oxidation of iron carbide by the oxidative products such as H_2O and CO_2 to the inactive iron oxide. This was confirmed by the activity measurement of pure-phase Fe_5C_2 treated with CO_2 at different temperatures (see Supporting Information Figure S9). Indeed, both the initial crystal phase of the catalyst and the reaction atmosphere could affect the structural evolution and eventually the equilibrium structure of iron-based catalysts under reaction conditions.

To rationalize the experimental results presented above, it is essential to study the intrinsic FTS activity of the pristine iron and the difference with the iron

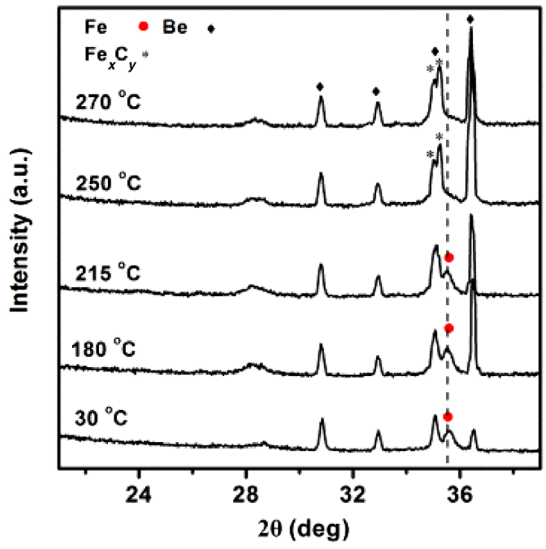

Figure 5 | *In situ XRD patterns of Fe NPs treated with 2 MPa syngas at various temperatures. (XRD was recorded in beam line 14B of SSRF. The diamonds mark the diffractions from beryllium-made in situ cell.)*

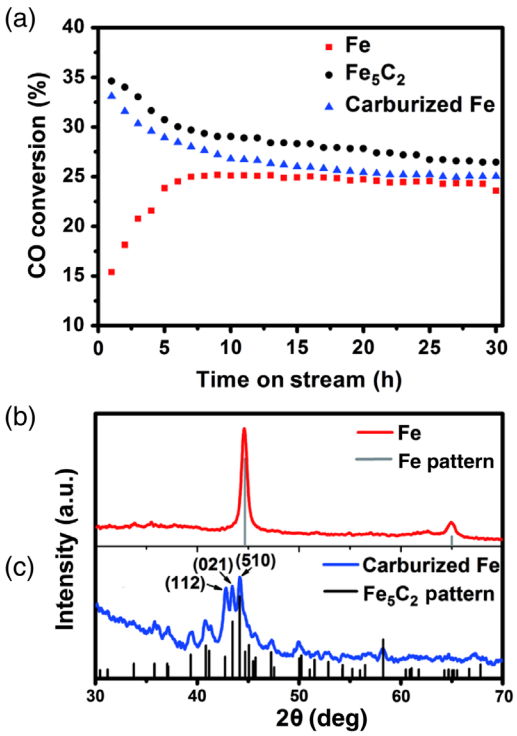

Figure 6 | *(a) CO conversion of α-Fe, Fe_5C_2, and precarburized α-Fe NPs catalysts. XRD pattern of α-Fe NPs catalysts (b) before and (c) after carburization. It is clear that carburizing the supported α-Fe catalyst with ethylene or the mixture of ethylene and hydrogen at 350 °C for 1 h would transform α-Fe to Fe_5C_2.*

DOI: 10.31635/ccschem.020.202000555
CCS Chem. **2020**, *2*, 2712–2724

carbide. Herein, DFT calculations were performed to study the crucial FTS steps including CO activation, C–C coupling and methane formation. The stepped Fe (310) and Fe-terminated Fe_5C_2 (100) surfaces (Supporting Information Figure S10) were used to model the corresponding iron and iron-carbides catalysts, respectively. The stepped Fe (310) was chosen here because the Fe (310) surface occupies a large proportion of surface area of the iron Wulff shape by 22%[67] and it shows higher activity for CO dissociation as compared with the traditional (110), (100), (211), and (111) surfaces.[68] Here, Fe_5C_2 (100) was selected since it is one of the largest exposed surfaces under operating FTS conditions (600 K, 10 bar, H_2/CO = 2.5) on Fe_5C_2 Wulff construction.[69] On a C-terminated Fe_5C_2 surface, there will be no active sites for CO activation or the activity of CO activation will be significant low.[70–72] Herein, we have adopted Fe-terminated Fe_5C_2 (100) surface which stands for the C-terminated Fe_5C_2 (100) surface with abundant C vacancies, where CO dissociation is feasible.[39,70] In addition, Fe (310) and Fe-terminated Fe_5C_2 (100) surfaces have the same B5 step surface, and it is feasible for the direct activity and selectivity comparison between Fe and Fe_5C_2.[73,74] The calculated binding energetics of the important intermediates CO*, C*, and CH* at their most favorable sites were –2.07, –8.15, and –6.90 eV on Fe (310), while –1.91, –7.08, and –6.53 eV on Fe_5C_2 (100) (Supporting Information Table S2), respectively. As expected, pristine iron is more reactive than iron carbide, and the binding strength toward C* is 1.07 eV stronger. This is determinative to the distinct activities of metal and carbide phases on CO activation, C–C coupling, and methane formation.

For Fe (310), calculated E_{app} for CO dissociation was 0.93 eV, with an exothermic reaction energy (–0.98 eV) due to the strong C–Fe binding (Figure 7a). The small barrier is in good accordance with observation of water formation at 150 °C. For C–C coupling, there are many possible pathways between CH_i and CH_j (i, j = 0–3). To evaluate their relative activity, equilibrium concentration of the corresponding monomers, which is proportional to their formation energy E_f (with zero-energy reference of CO dissociation product), should be considered. We define accordingly apparent barrier E_{app}, namely, summation of formation energy E_f of CH_i and CH_j and their coupling barrier E_c. It is found that the strong C–Fe binding not only makes the formation of CH_i and CH_j monomers energetically highly costly with E_f falling in a magnitude of 2.49 eV, but also makes CH_i–CH_j coupling kinetically very demanding with a maximum E_c of 1.99 eV (Table 2 and Supporting Information Figure S15). Indeed, among all possible CH_i–CH_j coupling considered, the least E_{app} (= E_f + E_c) calculated was as large as 1.87 eV from C*–CH* coupling. Methane formation was also found to be highly demanding with an overall barrier of 2.27 eV (Supporting Information Table S3 and Figure 8b).

The large barriers for C–C coupling and methane formation on Fe (310) lead to a rather poor FTS activity for the pristine iron. Our DFT calculations are also consistent with previous experimental results that iron catalysts containing no carbide have the lowest FTS activity.[28] The dissociated carbon from CO would therefore be sufficient for a long time on the catalyst surface, which is necessary for carburization and transition toward more thermodynamically favorable carbide. As a result, the unsaturated C_2 hydrocarbon observed on iron at 170 °C (Figure 4b) cannot come from the pristine iron. Instead, it comes from the carburized iron catalysts, namely, iron carbide. Since dissociated carbon was already available at 150 °C on the pristine iron, this also means the carburization process requires the activation temperature of at least 170 °C.

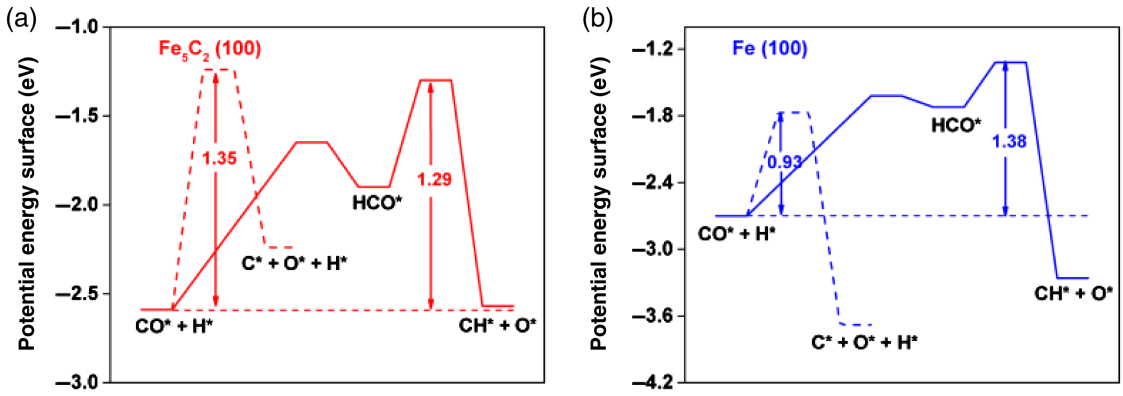

Figure 7 | *The potential energy diagrams for CO dissociation on (a) Fe_5C_2 (100) (red) and (b) Fe (310) (blue) surfaces. The solid and dashed lines present direct and H-assisted CO activation pathways, respectively. The apparent activation barriers (in eV) are indicated. The corresponding geometries involved in CO activation are shown in Supporting Information Figures S11 and S12.*

DOI: 10.31635/ccschem.020.202000555
CCS Chem. **2020**, *2*, 2712–2724

Table 2 | *Calculated Energetic for CH_x-CH_y Coupling over Fe_5C_2(100) and Fe(310) Surfaces.* E_f, E_c *and* E_{app} *are the Formation Energy of CH_x* and CH_y*, Elementary Coupling Barrier between CH_x* and CH_y*, and the Apparent Barrier on Fe_5C_2 (100) and Fe (310) Surfaces. The Formation Energy Was Calculated with Respect to CH* on Fe_5C_2 (100) Surface and the Atomic Carbon C* on the Fe (310) Surface Since They Are Located at the Lowest Valley of the Whole Potential Surface*

	Fe_5C_2 (100)			Fe (310)		
Reaction	E_c (eV)	E_f (eV)	E_{app} (eV)	E_c (eV)	E_f (eV)	E_{app} (eV)
C*–C*	0.84	0.47	1.31	1.99	0.00	1.99
C*–CH*	0.78	0.24	1.02	1.45	0.42	1.87
C*–CH_2*	0.77	0.59	1.36	1.16	1.20	2.36
C*–CH_3*	1.13	0.52	1.65	1.03	1.29	2.32
CH*–CH*	1.02	0.00	1.02	1.38	0.85	2.23
CH*–CH_2*	0.60	0.36	0.96	1.24	1.63	2.87
CH*–CH_3*	1.19	0.28	1.47	1.35	1.71	3.06
CH_2*–CH_2*	0.48	0.72	1.20	0.79	2.41	3.20
CH_2*–CH_3*	1.16	0.64	1.80	1.07	2.49	3.56

For Fe_5C_2 (100), the calculated E_{app} for CO dissociation is 1.29 eV with an endothermic reaction energy (Figure 7b), due to the destabilization of dissociated C* on the carbide surface. Though the CO dissociation barrier is higher than that of Fe (310), its modest value makes CO dissociation on Fe_5C_2 (100) remain facile, for instance at 150 °C. This is still in accordance with experimental observation of water formation at this temperature. On the other hand, the destabilization of surface C* and CH* on carbide (Supporting Information Table S2) greatly promotes the C–C coupling and methane formation. The formation of CH_i and CH_j monomers becomes energetically much less costly with E_f falling in the range of 0–0.72 eV, and the CH_i–CH_j coupling becoming kinetically facile with a maximum E_c of 1.19 eV (Table 2 and Supporting Information Figure S16). As a result, the least E_{app} calculated for the C–C coupling is only 0.96 eV from CH*–CH_2* coupling. Moreover, C*–CH*, CH*–CH*, and CH_2*–CH_2* coupling are also kinetically favorable with E_{app} of 1.02, 1.02, and 1.20 eV, respectively. For methane formation, the overall barrier also decreases significantly to 1.38 eV (Supporting Information Table S4 and Figure 8a).

As can be seen in the reaction barriers in Figure 9, C–C coupling barriers are even lower as compared with CO activation on Fe_5C_2 (100) with a barrier of 1.29 eV. This means once CO dissociates on Fe_5C_2, all these C–C coupling pathways could take place right away. This nicely corroborates the experiment with Fe_5C_2 at 150 °C (Figure 4a), namely, once syngas was activated, both acetylene and ethylene were observed simultaneously with the formation of water. Meanwhile, the barrier for

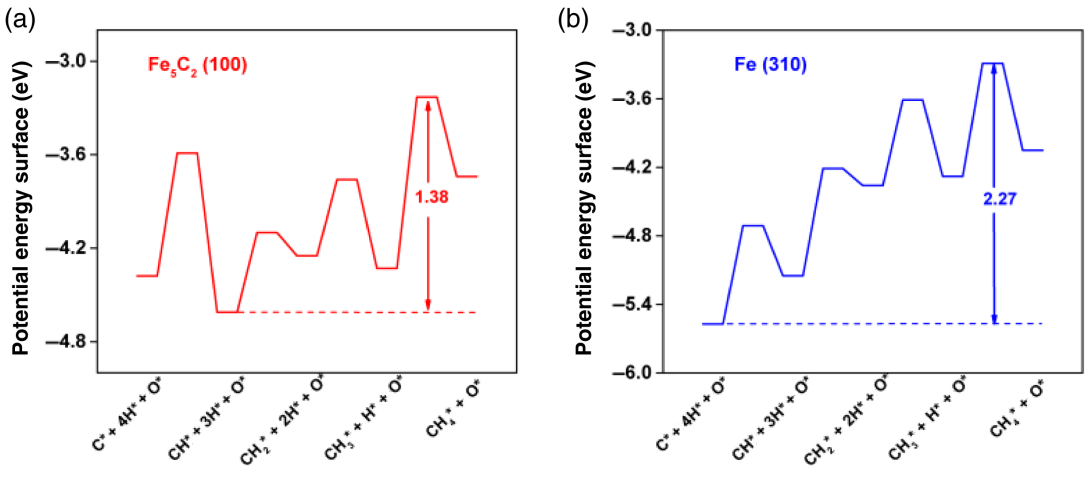

Figure 8 | *The potential energy diagram for methane formation on (a) Fe5C2 (100) (red) and (b) Fe (310) (blue) surfaces. The apparent activation barriers (in eV) are indicated. The corresponding configurations for intermediates adsorption and transition states are shown in Supporting Information Figure S13 and Figure S14, respectively.*

DOI: 10.31635/ccschem.020.202000555
CCS Chem. **2020**, *2*, 2712–2724

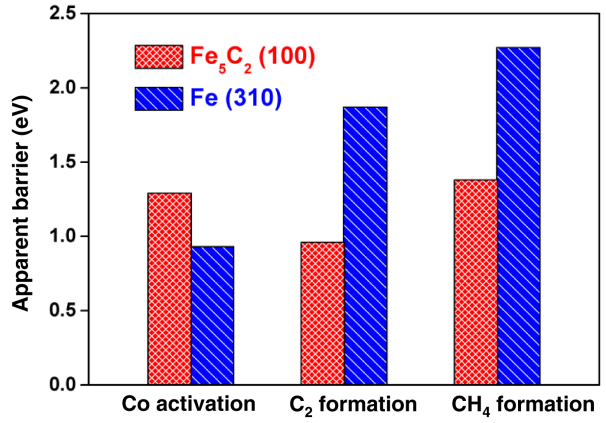

Figure 9 | *Apparent barriers comparison for CO activation, C_2, and CH_4 formation on Fe_5C_2 (100) and Fe (310) surfaces.*

methane formation remains higher than that of CO activation, a fact that was also the case with Fe (310). This implies that a higher temperature for methane formation would be required, which was indeed found in the corresponding STPSR experiment (Figure 4a).

Conclusion

Through a modified liquid-phase route, a series of pure-phase metallic iron and iron-carbide NPs were successfully synthesized, providing an ideal platform to investigate the fundamentals in an iron-based FTS reaction that has not previously been revealed. Fe_2C, Fe_7C_3, and Fe_5C_2 were all found to be active for FTS reaction, with Fe_5C_2 the most active phase. By using a house-designed STPSR method, transient information about the surface species and its reactivity was revealed. DFT calculations showed that iron carbide is intrinsically more active than the pristine iron for C–C coupling and methane formation because of the strong binding of dissociated atomic carbon on iron. Furthermore, C–C coupling was easier compared with methane formation on iron carbide, which makes iron carbide highly active for FTS with good olefin selectivity. The distinct activities of different iron phases (metal vs carbide) also revealed their stability under FTS conditions could be used to design more efficient iron-based FTS catalysts.

Additions and Corrections

a. Page 2712, The author list was incomplete in the original paper. Two names marked as bold below have to be added as the coauthors who did the Mössbauer Spectroscopy characterization.

"Huabo Zhao[1†], Jin-Xun Liu[2†], Ce Yang[3†], Siyu Yao[1], Hai-Yan Su[4], Zirui Gao[1], Mei Dong[5], **Junhu Wang[6], Alexandre I. Rykov[6]**, Jianguo Wang[5], Yanglong Hou[3*], Wei-Xue Li[2*] & Ding Ma[1*]

*[1]College of Chemistry and Molecular Engineering, Peking University, Beijing 100871, [2]Department of Chemical Physics, School of Chemistry and Materials Science, Hefei National Laboratory for Physical Sciences at the Microscale, iCHEM, University of Science and Technology of China, Hefei 230026, [3]Department of Materials Science and Engineering, College of Engineering, Peking University, Beijing 100871, [4]School of Chemical Engineering and Energy Technology, Dongguan University of Technology, Dongguan 523808, [5]State Key Laboratory of Coal Conversion, Institute of Coal Chemistry, Chinese Academy of Sciences, Taiyuan 030001, [6]**Center for Advanced Mössbauer Spectroscopy, Dalian Institute of Chemical Physics, Chinese Academy of Sciences, Dalian 116023**"*

b. Page 2721, The Acknowledgment Section in the original paper was missing, and should have appeared as shown below:

Acknowledgment:

Work supported by Mössbauer Effect Data Center, Dalian Institute of Chemical Physics, Chinese Academy of Sciences, China.

These changes were made post pulication on Mar. 8, 2021. All authors on the article are aware of and agree with the changes.

Supporting Information

Supporting Information is available and includes the XRD spectra (Figures S1 and S2); physical absorption characterization of the support material (Figure S3); Mössbauer effect spectra (Table S1 and Figure S4); products distribution of catalysts (Figure S5); TEM images and XRD patterns of used catalysts (Figures S6 and S7); TPSR of Fe and Fe_5C_2 in pure H_2 (Figure S8); XAFS spectra (Figure S9) and FTS performances of CO_2 treated Fe_5C_2 catalyst; energetic and geometric information for CO activation, CH_4 formation, and CH_x–CH_x coupling by DFT calculations (Tables S2–S4 and Figures S10–S16).

Conflict of Interest

There is no conflict of interest to report.

Funding Information

This work was financially supported by the Natural Science Foundation of China (nos. 21725301, 91645115, 21821004, 21932002, 51631001, 91645202, and 91945302), the National Key R&D Program of China (nos. 2017YFB0602200, 2017YFB0602205, and 2018YFA0208603), the Natural Science Foundation of Beijing Municipality (no. 2191001), and the Chinese

Academy of Sciences Key Project (no. QYZDJ-SSW-SLH054). XAS experiments were conducted at the Shanghai Synchrotron Radiation Facility (SSRF) and Beijing Synchrotron Radiation Facility (BSRF). XRD experiments were conducted at SSRF. The Super Computing Center of the University of Science and Technology of China (USTC) is gratefully acknowledged.

Acknowledgment

Work supported by Mössbauer Effect Data Center, Dalian Institute of Chemical Physics, Chinese Academy of Sciences, China.[b]

References

1. Dry, M. E. The Fischer–Tropsch (Ft) Synthesis Processes. Ertl, G.; Knözinger, H.; Schth, F.; Weitkamp, J. (eds.) In *Handbook of Heterogeneous Catalysis*; Wiley-VCH Verlag GmbH & Co. KGaA, Weinheim, Germany: **2008**; Vol. 13, p 2965.
2. Remans, T. J.; Jenzer, G.; Hoek, A. Gas-to-Liquids. In *Handbook of Heterogeneous Catalysis*; Wiley-VCH Verlag GmbH & Co. KGaA: **2008**; Vol. 13, p 2994.
3. de Smit, E.; Weckhuysen, B. M. The Renaissance of Iron-Based Fischer-Tropsch Synthesis: On the Multifaceted Catalyst Deactivation Behaviour. *Chem. Soc. Rev.* **2008**, *37*, 2758–2781.
4. Bukur, D. B.; Nowicki, L.; Manne, R. K.; Lang, X. Activation Studies with a Precipitated Iron Catalyst for Fischer-Tropsch Synthesis: II. Reaction Studies. *J. Catal.* **1995**, *155*, 366–375.
5. O'Brien, R. J.; Xu, L. G.; Spicer, R. L.; Davis, B. H. Activation Study of Precipitated Iron Fischer-Tropsch Catalysts. *Energ. Fuel.* **1996**, *10*, 921–926.
6. Bukur, D. B.; Okabe, K.; Rosynek, M. P.; Li, C.; Wang, D.; Rao, K.; Huffman, G. Activation Studies with a Precipitated Iron Catalyst for Fischer-Tropsch Synthesis: I. Characterization Studies. *J. Catal.* **1995**, *155*, 353–365.
7. Shroff, M. D.; Kalakkad, D. S.; Coulter, K. E.; Kohler, S. D.; Harrington, M. S.; Jackson, N. B.; Sault, A. G.; Datye, A. K. Activation of Precipitated Iron Fischer-Tropsch Synthesis Catalysts. *J. Catal.* **1995**, *156*, 185–207.
8. Eliason, S.; Bartholomew, C. Reaction and Deactivation Kinetics for Fischer–Tropsch Synthesis on Unpromoted and Potassium-Promoted Iron Catalysts. *Appl. Catal. A* **1999**, *186*, 229–243.
9. Moyer, M. M.; Karakaya, C.; Kee, R. J.; Trewyn, B. G. In Situ Formation of Metal Carbide Catalysts. *ChemCatChem* **2017**, *9*, 3090–3101.
10. Yang, X.; Zhang, H.; Liu, Y.; Ning, W.; Han, W.; Liu, H.; Huo, C. Preparation of Iron Carbides Formed by Iron Oxalate Carburization for Fischer–Tropsch Synthesis. *Catalysts* **2019**, *9*, 347.
11. Liaw, S. J.; Davis, B. H. Fischer-Tropsch Synthesis. Compositional Changes in an Iron Catalyst During Activation and Use. *Top. Catal.* **2000**, *10*, 133–139.
12. Li, S. Z.; Meitzner, G. D.; Iglesia, E. Structure and Site Evolution of Iron Oxide Catalyst Precursors during the Fischer-Tropsch Synthesis. *J. Phys. Chem. B* **2001**, *105*, 5743–5750.
13. Perez-Alonso, F. J.; Herranz, T.; Rojas, S.; Ojeda, M.; Lopez Granados, M.; Terreros, P.; Fierro, J. L. G.; Gracia, M.; Gancedo, J. R. Evolution of the Bulk Structure and Surface Species on Fe-Ce Catalysts during the Fischer-Tropsch Synthesis. *Green Chem.* **2007**, *9*, 663–670.
14. de Smit, E.; Swart, I.; Creemer, J. F.; Hoveling, G. H.; Gilles, M. K.; Tyliszczak, T.; Kooyman, P. J.; Zandbergen, H. W.; Morin, C.; Weckhuysen, B. M. Nanoscale Chemical Imaging of a Working Catalyst by Scanning Transmission X-Ray Microscopy. *Nature* **2008**, *456*, 222–225.
15. Janbroers, S.; Louwen, J. N.; Zandbergen, H. W.; Kooyman, P. J. Insights into the Nature of Iron-Based Fischer-Tropsch Catalysts from Quasi in Situ Tem-Eels and XRD. *J. Catal.* **2009**, *268*, 235–242.
16. Fjellvag, H.; Karen, P. Crystal-Structure of Magnesium Sesquicarbide. *Inorg. Chem.* **1992**, *31*, 3260–3263.
17. Ferrari, A. C.; Meyer, J.; Scardaci, V.; Casiraghi, C.; Lazzeri, M.; Mauri, F.; Piscanec, S.; Jiang, D.; Novoselov, K.; Roth, S. Raman Spectrum of Graphene and Graphene Layers. *Phys. Rev. Lett.* **2006**, *97*, 187401.
18. Sun, L. D.; Jia, C. J.; Luo, F.; Han, X. D.; Heyderman, L. J.; Yan, Z. G.; Yan, C. H.; Zheng, K.; Zhang, Z.; Takano, M.; Hayashi, N.; Eltschka, M.; Klaui, M.; Rudiger, U.; Kasama, T.; Cervera-Gontard, L.; Dunin-Borkowski, R. E.; Tzvetkov, G.; Raabe, J. Large-Scale Synthesis of Single-Crystalline Iron Oxide Magnetic Nanorings. *J. Am. Chem. Soc.* **2008**, *130*, 16968–16977.
19. Yang, C.; Zhao, H. B.; Hou, Y. L.; Ma, D. Fe_5C_2 Nanoparticles: A Facile Bromide-Induced Synthesis and as an Active Phase for Fischer-Tropsch Synthesis. *J. Am. Chem. Soc.* **2012**, *134*, 15814–15821.
20. Liu, X.-W.; Cao, Z.; Zhao, S.; Gao, R.; Meng, Y.; Zhu, J.-X.; Rogers, C.; Huo, C.-F.; Yang, Y.; Li, Y.-W. Iron Carbides in Fischer–Tropsch Synthesis: Theoretical and Experimental Understanding in Epsilon-Iron Carbide Phase Assignment. *J. Phys. Chem. C* **2017**, *121*, 21390–21396.
21. Wezendonk, T. A.; Sun, X.; Dugulan, A. I.; van Hoof, A. J.; Hensen, E. J.; Kapteijn, F.; Gascon, J. Controlled Formation of Iron Carbides and Their Performance in Fischer-Tropsch Synthesis. *J. Catal.* **2018**, *362*, 106–117.
22. Wang, P.; Chen, W.; Chiang, F.-K.; Dugulan, A. I.; Song, Y.; Pestman, R.; Zhang, K.; Yao, J.; Feng, B.; Miao, P. Synthesis of Stable and Low-CO_2 Selective E-Iron Carbide Fischer-Tropsch Catalysts. *Sci. Adv.* **2018**, *4*, eaau2947.
23. Kuei, C.-K.; Lee, M.-D. Temperature-Programmed Reaction of Pre-Adsorbed CO on Iron Catalyst: New Experimental Evidence for Competition Model. *J. Mol. Catal.* **1991**, *65*, 293–305.
24. Niemantsverdriet, J.; Van der Kraan, A.; Van Dijk, W.; Van der Baan, H. Behavior of Metallic Iron Catalysts during Fischer-Tropsch Synthesis Studied with Mossbauer Spectroscopy, X-Ray Diffraction, Carbon Content Determination, and Reaction Kinetic Measurements. *J. Phys. Chem.* **2002**, *84*, 3363–3370.
25. Amelse, J. A.; Butt, J. B.; Schwartz, L. H. Carburization of Supported Iron Synthesis Catalysts. *J. Phys. Chem.* **1978**, *82*, 558–563.

DOI: 10.31635/ccschem.020.202000555
CCS Chem. **2020**, *2*, 2712–2724

26. Rao, K. R. P. M.; Huggins, F. E.; Ganguly, B.; Mahajan, V.; Huffman, G. P.; Davis, B.; Obrien, R. J.; Xu, L. G.; Rao, V. U. S. Effect of Pre-Heat Treatment on a Fischer-Tropsch Iron Catalyst. *Hyperfine Interact.* **1994**, *93*, 1755–1758.
27. Badani, M. V.; Delgass, W. N. The Active Phase of Iron Catalysts for Acetonitrile Synthesis. *J. Catal.* **1999**, *187*, 506–517.
28. Mansker, L. D.; Jin, Y.; Bukur, D. B.; Datye, A. K. Characterization of Slurry Phase Iron Catalysts for Fischer–Tropsch Synthesis. *Appl. Catal. A* **1999**, *186*, 277–296.
29. Schulz, H.; Riedel, T.; Schaub, G. Fischer-Tropsch Principles of CO-Hydrogenation on Iron Catalysts. *Top. Catal.* **2005**, *32*, 117–124.
30. Herranz, T.; Rojas, S.; Perez-Alonso, F. J.; Ojeda, M.; Terreros, P.; Fierro, J. L. G. Genesis of Iron Carbides and Their Role in the Synthesis of Hydrocarbons from Synthesis Gas. *J. Catal.* **2006**, *243*, 199–211.
31. Hao, Q. L.; Bai, L.; Xiang, H. W.; Li, Y. W. Phase Transformations of a Spray-Dried Iron Catalyst for Slurry Fischer-Tropsch Synthesis during Activation and Reaction. *Fuel Process. Technol.* **2008**, *89*, 1358–1364.
32. de Smit, E.; Cinquini, F.; Beale, A. M.; Safonova, O. V.; van Beek, W.; Sautet, P.; Weckhuysen, B. M. Stability and Reactivity of Epsilon-Chi-Theta Iron Carbide Catalyst Phases in Fischer-Tropsch Synthesis: Controlling μ(C). *J. Am. Chem. Soc.* **2010**, *132*, 14928–14941.
33. Torres Galvis, H. M.; Bitter, J. H.; Khare, C. B.; Ruitenbeek, M.; Dugulan, A. I.; de Jong, K. P. Supported Iron Nanoparticles as Catalysts for Sustainable Production of Lower Olefins. *Science* **2012**, *335*, 835–838.
34. Yang, C.; Zhao, B.; Gao, R.; Yao, S.; Zhai, P.; Li, S.; Yu, J.; Hou, Y.; Ma, D. Construction of Synergistic Fe_5C_2/Co Heterostructured Nanoparticles as an Enhanced Low Temperature Fischer–Tropsch Synthesis Catalyst. *ACS Catal.* **2017**, *7*, 5661–5667.
35. Gao, R.; Liu, X.; Cao, Z.; Liu, X.-W.; Lu, K.; Ma, D.; Yang, Y.; Li, Y.-W.; Hoffmann, R.; Wen, X.-D. Carbon Permeation: The Prerequisite Elementary Step in Iron-Catalyzed Fischer–Tropsch Synthesis. *Catal. Lett.* **2019**, *149*, 645–664.
36. Chang, Q.; Zhang, C.; Liu, C.; Wei, Y.; Cheruvathur, A. V.; Dugulan, A. I.; Niemantsverdriet, J.; Liu, X.; He, Y.; Qing, M. Relationship between Iron Carbide Phases (ε-Fe_2C, Fe_7C_3, and X-Fe_5C_2) and Catalytic Performances of Fe/Sio_2 Fischer–Tropsch Catalysts. *ACS Catal.* **2018**, *8*, 3304–3316.
37. Lu, F.; Chen, X.; Lei, Z.; Wen, L.; Zhang, Y. Revealing the Activity of Different Iron Carbides for Fischer-Tropsch Synthesis. *Appl. Catal. B* **2020**, *281*, 119521.
38. Zhuo, O.; Yang, L.; Gao, F.; Xu, B.; Wu, Q.; Fan, Y.; Zhang, Y.; Jiang, Y.; Huang, R.; Wang, X.; Hu, Z. Stabilizing the Active Phase of Iron-Based Fischer–Tropsch Catalysts for Lower Olefins: Mechanism and Strategy. *Chem. Sci.* **2019**, *10*, 6083–6090.
39. Huo, C.-F.; Li, Y.-W.; Wang, J.; Jiao, H. Insight into CH_4 Formation in Iron-Catalyzed Fischer–Tropsch Synthesis. *J. Am. Chem. Soc.* **2009**, *131*, 14713–14721.
40. Cheng, J.; Hu, P.; Ellis, P.; French, S.; Kelly, G.; Lok, C. M. An Energy Descriptor to Quantify Methane Selectivity in Fischer-Tropsch Synthesis: A Density Functional Theory Study. *J. Phys. Chem. C* **2009**, *113*, 8858–8863.
41. Ojeda, M.; Nabar, R.; Nilekar, A. U.; Ishikawa, A.; Mavrikakis, M.; Iglesia, E. CO Activation Pathways and the Mechanism of Fischer-Tropsch Synthesis. *J. Catal.* **2010**, *272*, 287–297.
42. Shetty, S. G.; Ciobica, I. M.; Hensen, E. J. M.; van Santen, R. A. Site Regeneration in the Fischer-Tropsch Synthesis Reaction: A Synchronized CO Dissociation and C-C Coupling Pathway. *Chem. Commun.* **2011**, *47*, 9822–9824.
43. Pham, T. H.; Duan, X.; Qian, G.; Zhou, X.; Chen, D. Co Activation Pathways of Fischer–Tropsch Synthesis on X-Fe_5C_2 (510): Direct Versus Hydrogen-Assisted CO Dissociation. *J. Phys. Chem. C* **2014**, *118*, 10170–10176.
44. Chen, W.; Filot, I. A.; Pestman, R.; Hensen, E. J. Mechanism of Cobalt-Catalyzed CO Hydrogenation: 2. Fischer–Tropsch Synthesis. *ACS Catal.* **2017**, *7*, 8061–8071.
45. Rivera de la Cruz, J. G.; Sabbe, M. K.; Reyniers, M.-F. First Principle Study on the Adsorption of Hydrocarbon Chains Involved in Fischer–Tropsch Synthesis over Iron Carbides. *J. Phys. Chem. C* **2017**, *121*, 25052–25063.
46. Kresse, G.; Hafner, J. Ab Initio Molecular Dynamics for Liquid Metals. *Phys. Rev. B* **1993**, *47*, 558.
47. Kresse, G.; Furthmüller, J. Efficient Iterative Schemes for Ab Initio Total-Energy Calculations Using a Plane-Wave Basis Set. *Phys. Rev. B* **1996**, *54*, 11169.
48. Kresse, G.; Joubert, D. From Ultrasoft Pseudopotentials to the Projector Augmented-Wave Method. *Phys. Rev. B* **1999**, *59*, 1758.
49. Perdew, J. P.; Burke, K.; Ernzerhof, M. Generalized Gradient Approximation Made Simple. *Phys. Rev. Lett.* **1996**, *77*, 3865–3868.
50. Monkhorst, H. J.; Pack, J. D. Special Points for Brillouin-Zone Integrations. *Phys. Rev. B* **1976**, *13*, 5188–5192.
51. Retief, J. J. Powder Diffraction Data and Rietveld Refinement of Hägg-Carbide, X-Fe_5C_2. *Powder Diffr.* **1999**, *14*, 130–132.
52. Kittel, C.; McEuen, P. *Introduction to Solid State Physics*; Wiley: New York, **1996**; Vol. 8, p20.
53. Sun, K.; Zhao, Y.; Su, H. Y.; Li, W. X. Force Reversed Method for Locating Transition States. *Theor. Chem. Acc.* **2012**, *131*, 1–10.
54. Henkelman, G.; Uberuaga, B. P.; Jónsson, H. A Climbing Image Nudged Elastic Band Method for Finding Saddle Points and Minimum Energy Paths. *J. Chem. Phys.* **2000**, *113*, 9901.
55. Yu, G.; Sun, B.; Pei, Y.; Xie, S.; Yan, S.; Qiao, M.; Fan, K.; Zhang, X.; Zong, B. Fe_XO_Y@C Spheres as an Excellent Catalyst for Fischer–Tropsch Synthesis. *J. Am. Chem. Soc.* **2010**, *132*, 935–937.
56. van Steen, E.; Claeys, M. Fischer-Tropsch Catalysts for the Biomass-to-Liquid (BTL)-Process. *Chem. Eng. Technol.* **2008**, *31*, 655–666.
57. Chen, W.; Fan, Z.; Pan, X.; Bao, X. Effect of Confinement in Carbon Nanotubes on the Activity of Fischer–Tropsch Iron Catalyst. *J. Am. Chem. Soc.* **2008**, *130*, 9414–9419.

DOI: 10.31635/ccschem.020.202000555
CCS Chem. **2020**, *2*, 2712–2724

58. Santos, V. P.; Wezendonk, T. A.; Jaén, J. J. D.; Dugulan, A. I.; Nasalevich, M. A.; Islam, H.-U.; Chojecki, A.; Sartipi, S.; Sun, X.; Hakeem, A. A. Metal Organic Framework-Mediated Synthesis of Highly Active and Stable Fischer-Tropsch Catalysts. *Nat. Commun.* **2015**, *6*, 6451.
59. Xu, K.; Sun, B.; Lin, J.; Wen, W.; Pei, Y.; Yan, S.; Qiao, M.; Zhang, X.; Zong, B. ε-Iron Carbide as a Low-Temperature Fischer–Tropsch Synthesis Catalyst. *Nat. Commun.* **2014**, *5*, 1–8.
60. Ma, D.; Shu, Y. Y.; Cheng, M. J.; Xu, Y. D.; Bao, X. H. On the Induction Period of Methane Aromatization over Mo-Based Catalysts. *J. Catal.* **2000**, *194*, 105–114.
61. Ma, D.; Wang, D.; Su, L.; Shu, Y.; Xu, Y.; Bao, X. Carbonaceous Deposition on Mo/HMCM-22 Catalysts for Methane Aromatization: A Tp Technique Investigation. *J. Catal.* **2002**, *208*, 260–269.
62. van Santen, R. A.; Ciobica, I. M.; van Steen, E.; Ghouri, M. M. Mechanistic Issues in Fischer-Tropsch Catalysis. *Adv. Catal.* **2011**, *54*, 127–187.
63. Van Santen, R.; Markvoort, A.; Filot, I.; Ghouri, M.; Hensen, E. Mechanism and Microkinetics of the Fischer–Tropsch Reaction. *Phys. Chem. Chem. Phys.* **2013**, *15*, 17038–17063.
64. Zhou, X.; Mannie, G. J. A.; Yin, J.; Yu, X.; Weststrate, C. J.; Wen, X.; Wu, K.; Yang, Y.; Li, Y.; Niemantsverdriet, J. W. Iron Carbidization on Thin-Film Silica and Silicon: A Near-Ambient-Pressure X-Ray Photoelectron Spectroscopy and Scanning Tunneling Microscopy Study. *ACS Catal.* **2018**, *8*, 7326–7333.
65. Erley, W.; McBreen, P. H.; Ibach, H. Evidence for CH_x Surface Species after the Hydrogenation of CO over an Fe(110) Single Crystal Surface. *J. Catal.* **1983**, *84*, 229–234.
66. Hwang, H.-S.; Chung, U.-C.; Chung, W.-S.; Cho, Y.-R.; Jung, B.-H.; Martin, G. P. Carburization of Iron Using CO –H_2 Gas Mixture. *Met. Mater. Int.* **2004**, *10*, 77–82.
67. Huo, C.-F.; Wu, B.-S.; Gao, P.; Yang, Y.; Li, Y.-W.; Jiao, H. The Mechanism of Potassium Promoter: Enhancing the Stability of Active Surfaces. *Angew. Chem. Int. Ed.* **2011**, *50*, 7403–7406.
68. Sorescu, D. C. Plane-Wave DFT Investigations of the Adsorption, Diffusion, and Activation of CO on Kinked Fe(710) and Fe(310) Surfaces. *J. Phys. Chem. C* **2008**, *112*, 10472–10489.
69. Zhao, S.; Liu, X.-W.; Huo, C.-F.; Li, Y.-W.; Wang, J.; Jiao, H. Surface Morphology of Hägg Iron Carbide (X-Fe_5C_2) from Ab Initio Atomistic Thermodynamics. *J. Catal.* **2012**, *294*, 47–53.
70. Ozbek, M. O.; Niemantsverdriet, J. W. Elementary Reactions of CO and H_2 on C-Terminated X-Fe_5C_2(001) Surfaces. *J. Catal.* **2014**, *317*, 158–166.
71. Broos, R. J. P.; Zijlstra, B.; Filot, I. A. W.; Hensen, E. J. M. Quantum-Chemical DFT Study of Direct and H- and C-Assisted CO Dissociation on the X-Fe_5C_2 Hägg Carbide. *J. Phys. Chem. C* **2018**, *122*, 9929–9938.
72. Li, T.; Wen, X.; Yang, Y.; Li, Y.-W.; Jiao, H. Mechanistic Aspects of CO Activation and C–C Bond Formation on the Fe/C- and Fe-Terminated Fe_3C(010) Surfaces. *ACS Catal.* **2020**, *10*, 877–890.
73. Cao, D.-B.; Zhang, F.-Q.; Li, Y.-W.; Jiao, H. Density Functional Theory Study of CO Adsorption on Fe_5C_2(001), -(100), and -(110) Surfaces. *J. Phys. Chem. B* **2004**, *108*, 9094–9104.
74. Elahifard, M. R.; Pérez Jigato, M.; Niemantsverdriet, J. W. Ab-Initio Calculations of the Direct and Hydrogen-Assisted Dissociation of CO on Fe(310). *Chem. Phys. Lett.* **2012**, *534*, 54–57.

DOI: 10.31635/ccschem.020.202000555
CCS Chem. **2020**, *2*, 2712–2724